

Direct Synthesis of ZIF-8 on Transmission Electron Microscopy Grids Allows Structure Analysis and 3D Reconstruction

Milena Hugenschmidt,* Ksenia Kutonova, Elvia P. Valadez Sánchez, Sarah Moulai, Hartmut Gliemann, Stefan Bräse, Christof Wöll, and Dagmar Gerthsen

The first example of layer-by-layer growth of a metal–organic framework (MOF) directly on transmission electron microscopy (TEM) grids is described. ZIF-8 is deposited on thin amorphous carbon films and subjected to a structure analysis by (scanning) TEM ((S)TEM). This method serves as a two-in-one synthesis and TEM sample-preparation technique and allows straightforward analysis of ZIF-8 crystallites. Artifacts resulting from sample preparation are completely avoided by this approach. The morphological properties, crystal structure, and the chemical composition of the material are investigated with high spatial resolution by a variety of methods of (analytical) electron microscopy. Furthermore, the incorporation of metallic nanoparticles in ZIF-8 by integrating a corresponding step into the layer-by-layer deposition process is examined. The formation of ZIF-8 crystals on the film proceeds as under the absence of nanoparticle-forming synthesis steps. However, the nanoparticles rather cover the supporting amorphous carbon film than being incorporated in the ZIF-8 material. This information cannot be obtained from standard characterization techniques but requires the application of analytical (S)TEM techniques.

large pore volume and high surface area.^[1–3] ZIF-8, pioneered by the group of Yaghi in 2006,^[4] is synthesized from commercially available sources: 2-methyl imidazole (Hmim), serving as a linker, and zinc salts, giving Zn²⁺ cations as nodes. Various synthetic methods for the formation of ZIF-8 have been reported. Those include different strategies toward powder ZIF-8,^[1–18] as well as layer-by-layer (lbl) approaches leading to ZIF-8 deposited on supports.^[19–23] The latter allow the synthesis of monolithic surface-anchored thin films of ZIF-8 (ZIF-8 SURMOF). Such surface-anchored MOFs (SURMOFs) show a high degree of crystallite orientation, controllable thickness, low defect densities, and therefore carry a high potential for thin-film applications.^[22,23]


In the recent past it has been recognized that, due to their permanent porosity, MOFs are perfect hosts for the incorporation of different guest species inside their pores,^[24–26] including metal nanoparticles (mNPs).^[27–31] For example, Esken et al. have prepared a Au/ZIF-8 composite by the ship-in-the-bottle method, where volatile [Au(CO)Cl] was immobilized into ZIF-8 by gas-phase infiltration, and then reduced by CO to form Au NPs/ZIF-8.^[32] Very recently, ZIF-8 with imbedded Ag/AgCl nanoparticles

1. Introduction

Zeolitic imidazolate frameworks (ZIFs) belong to the material class of metal–organic frameworks (MOFs). ZIFs are structurally isomorphous to zeolites, and in particular ZIF-8 has fascinating properties such as high thermal and chemical stability,

M. Hugenschmidt, Prof. D. Gerthsen
Laboratory for Electron Microscopy (LEM)
Karlsruhe Institute of Technology
Engesserstr. 7, Karlsruhe 76131, Germany
E-mail: milena.hugenschmidt@kit.edu

M. Hugenschmidt, Dr. K. Kutonova, Prof. S. Bräse, Prof. D. Gerthsen
Material Research Center for Energy Systems (MZE)
Karlsruhe Institute of Technology
Strasse am Forum 7, Karlsruhe 76131, Germany

 The ORCID identification number(s) for the author(s) of this article can be found under <https://doi.org/10.1002/ppsc.202000209>.

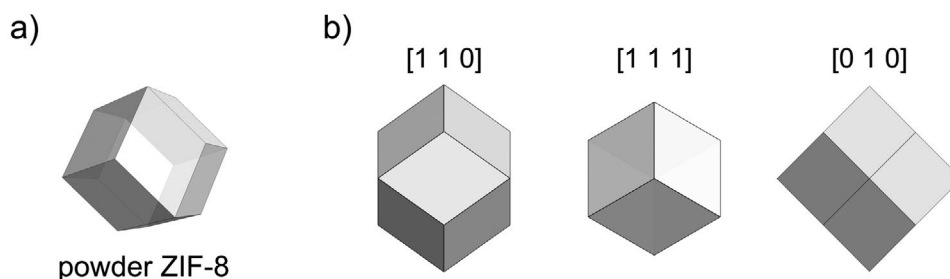
© 2020 The Authors. Published by Wiley-VCH GmbH. This is an open access article under the terms of the Creative Commons Attribution License, which permits use, distribution and reproduction in any medium, provided the original work is properly cited.

DOI: 10.1002/ppsc.202000209

Dr. K. Kutonova, Prof. S. Bräse
Institute of Organic Chemistry (IOC)
Karlsruhe Institute of Technology
Fritz-Haber-Weg 6, Karlsruhe 76131, Germany

Dr. E. P. Valadez Sánchez, S. Moulai, Dr. H. Gliemann, Prof. C. Wöll
Institute of Functional Interfaces (IFG), Karlsruhe Institute of Technology
Hermann-von-Helmholtz-Platz 1
Eggenstein-Leopoldshafen 76344, Germany

Prof. S. Bräse
Institute of Biological and Chemical Systems (IBCS-FMS)
Karlsruhe Institute of Technology
Hermann-von-Helmholtz-Platz 1
Eggenstein-Leopoldshafen 76344, Germany



Scheme 1. a) Scheme of the rhombic dodecahedron (RD) shape of powder ZIF-8. b) Views of the RD shape along different low-index projections.

was prepared by the one-pot method, combining nucleation, precipitation, growth and photoreduction.^[33] The characterization of such complex composites required the combination of several analytical techniques. Besides X-ray diffraction, adsorption–desorption experiments and infrared spectroscopy, electron microscopy techniques were intensively used to demonstrate the successful synthesis.

Electron microscopy is a frequently applied method for the characterization of MOFs and mNPs/MOF composites because it provides essential information on the (nano)structure and local chemical composition. It is particularly indispensable for the structural and chemical characterization of small material quantities because X-ray diffraction (XRD) and CHNX elemental analysis cannot be performed.

Electron microscopy is also a powerful tool for the understanding of MOFs formation process. Thus, it is known from scanning electron microscopy (SEM) studies that powder ZIF-8 crystals pass through different growth stages during synthesis, characterized by different crystal shapes, at least in aqueous and methanolic formate modulated solvothermal synthesis.^[34,35] The structure formation process starts with a cubic particle shape and yields a rhombic dodecahedron (RD) in the final state, where all side faces expose {110} planes (**Scheme 1a**).^[35,36] Scheme 1b shows RD crystals along different low-index projections, which can be recognized by SEM.^[9,34,35,37]

Transmission electron microscopy (TEM) and scanning transmission electron microscopy (STEM) have been used to study the shape and structure of ZIF-8 particles at higher resolution.^[37,38] High-resolution (HR)STEM and high-resolution (HR)TEM reveal details on the crystallinity and atomic structure as well as on the orientation of ZIF-8 crystals.^[9,39,40] Electron diffraction is another versatile technique to investigate the crystalline structure of particle ensembles and even single particles of ZIF-8.^[32,37,41] Energy-dispersive X-ray spectroscopy (EDXS), especially elemental mapping, in a transmission electron microscope was used to analyze the chemical composition of ZIF-8/ZIF-67 composite at high spatial resolution.^[38] The 3D shape of ZIF-8 particles and the distribution of Au NPs imbedded in ZIF-8 were reconstructed by TEM tomography.^[32]

The cited works on (S)TEM discuss the structure of ZIF-8 and mNP/ZIF-8 composites, prepared in the form of powder. (S)TEM studies on lbl-grown ZIF-8 have not yet been reported up to now. Only a few studies on other lbl-fabricated MOFs using (S)TEM have been published.^[42–46] These reports do not contain HR(S)TEM images that reveal the crystalline structure of the material, most likely due to the lack of suitable TEM sample preparation techniques. Since the lbl process yields thin films deposited on solid substrates, they must be detached from

the surface and then deposited on the TEM grids. By detaching the SURMOF from the bulk substrate, for example by PMMA-assisted shaving or a laser-ablation process,^[43,45] the material can be damaged and important structural information may be lost. For example, amorphization and contamination may occur during TEM sample preparation, and it is then impossible to conclude whether the observed SURMOF structure stems from the synthesis or the detachment procedure.

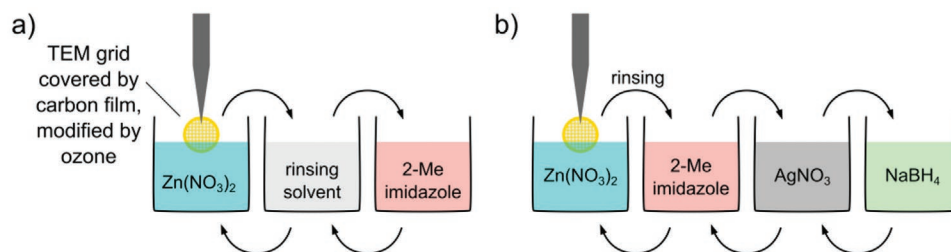
In this work, we report the successful lbl growth of ZIF-8 on commercially available TEM grids, which consist of a thin amorphous carbon (aC) film supported by a Cu grid. Those grids are widely used in electron microscopy and are well suited for (S) TEM investigations. The characterization of the material can start directly after its preparation using lbl deposition without any further preparation steps for TEM, which prevents the modification of the original structural and chemical properties. We have applied a broad range of SEM and (S)TEM techniques to analyze the morphology, structural and chemical properties of the lbl-grown ZIF-8. The suggested procedure facilitates (S) TEM studies of SURMOFs in the future, which are up now scarce due to the lack of adequate TEM sample preparation procedures. In addition, we test a new synthesis route to incorporate Ag NPs in ZIF-8 where electron microscopy yields decisive information on the distribution and location of Ag NPs, which is not available from other standard characterization techniques.

2. Results

2.1. Synthesis

ZIF-8 in the form of SURMOF was synthesized directly on the aC-covered TEM grid by the lbl method, similar to the previously reported technique.^[22,23] We note that the term lbl does not imply planar growth, where a closed ZIF-8 layer is formed from the start of the deposition. It rather refers to the precise control of the amount of deposited material by the number of deposition cycles.^[47]

For this, methanolic solutions of zinc nitrate (node) and Hmim (linker) were prepared. An aC-covered TEM grid freshly modified by UV/ozone plasma was immersed in those solutions, with rinsing steps in pure MeOH in between (**Scheme 2a**). Since SURMOF-coated TEM grids are too small for direct investigation by powder X-ray diffraction (pXRD) and other standard characterization methods, macroscopic substrates with an –OH terminated surface (11-mercapto-1-undecanol self-assembled monolayer (MUD SAM)), chemically comparable with that of the UV/ozone plasma-treated aC-covered



Scheme 2. Layer-by-layer fabrication of ZIF-8 on an aC-covered TEM grid via dipping: a) ZIF-8 synthesis, b) Ag/ZIF-8 synthesis.

TEM grids, were prepared for the ZIF-8 growth. Characterization by pXRD of the macroscopic sample, prepared in parallel, reveals the formation of the crystalline ZIF-8 with predominant (110) orientation (Figure S1, Supporting Information).

Additionally, a new method for the synthesis of a mNPs and ZIF-8 composite (mNPs/ZIF-8) was explored, combining the lbl approach for the synthesis of ZIF-8 and ship-in-the-bottle liquid impregnation method for the formation of the mNPs. In this approach, Ag NPs were used as a model system. This lbl ship-in-the-bottle approach implies that the substrate for the Ag NPs—silver nitrate—diffuses inside the pores of ZIF-8 during its deposition and is consequently chemically reduced by NaBH_4 to metallic Ag NPs. The system $\text{AgNO}_3/\text{NaBH}_4$ has been previously reported in the literature and successfully utilized for the synthesis of Ag/ZIF-8,^[48] as well as Ag/MIL-101.^[49] Thus, for the preparation of Ag/ZIF-8 SURMOF, two additional steps were added in the lbl process with rinsing steps in pure MeOH in between: 1) immersion into the methanolic solution of AgNO_3 , which serves as precursor solution for the Ag NPs, and 2) immersion into the methanolic solution of NaBH_4 , causing the reduction of AgNO_3 and formation of metallic Ag NPs. This new approach of lbl ship-in-the-bottle liquid impregnation method is schematically shown in Scheme 2b.

Besides the SURMOF growth on aC-covered TEM grids, macroscopic substrates were used for mNPs/ZIF-8 preparation. Characterization by pXRD, infrared reflection absorption spectroscopy (IRRAS), time-of-flight secondary ion mass spectrometry (ToF-SIMS) and X-ray photoelectron spectroscopy (XPS) analysis of these macroscopic samples support the presence of Ag in the metallic state and also crystallinity of ZIF-8 (Figures S1–S4, Supporting Information).

2.2. Morphology

SEM was used to analyze the morphology of ZIF-8 grown on thin aC films. **Figure 1** shows the typical appearance of ZIF-8 crystallites after 50 cycles of lbl growth. Isolated ZIF-8 particles with sizes between a few 10 nm and around 250 nm are observed. At this stage, separated ZIF-8 particles are formed without full coverage of the aC film (Figure 1a). A high-magnification image of this sample reveals the characteristic particle shapes in more detail (Figure 1b). We note that we did not observe a significant difference in size and morphology of ZIF-8 particles grown on macroscopic substrates and TEM grids, as shown in Figure S8, Supporting Information. The strong faceting of the RD particles suggests that they are crystalline. To facilitate the comparison of the particles with the

expected RD shape, the edges of three particles are traced with black lines. Low-index projections of the RD shape are observed (cf. Scheme 1b) and are labeled accordingly. Some of the smaller particles are more rounded compared to the bigger ones. This difference in the size and shape of ZIF-8 crystals after 50 deposition cycles indicates that during our lbl method ZIF-8 crystals also pass through different growth stages, as it is reported for the powder ZIF-8 synthesis and discussed above.

After 100 deposition cycles (**Figure 2**), the morphology of the ZIF-8 on aC film has changed. The SEM image Figure 2a taken with the through-lens detector (TLD) shows the surface topography of the ZIF-8. After this larger number of deposition

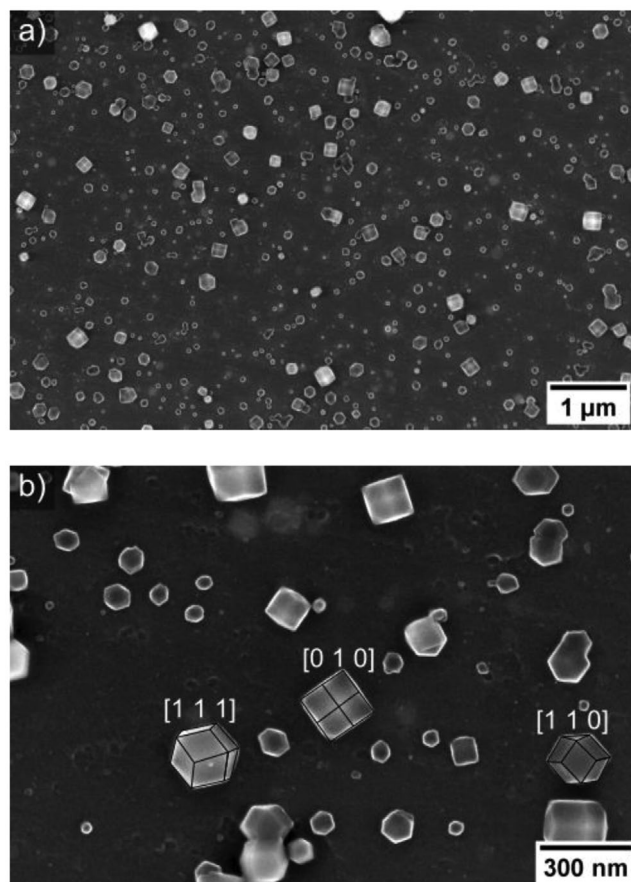


Figure 1. Secondary-electron SEM micrographs of ZIF-8 obtained from layer-by-layer growth after 50 deposition cycles. a) Overview image, b) higher-magnification image, which shows low-index projections of RD particles. For clarity, the particle edges are traced with black lines. Both images were taken at 5 keV primary electron energy with the through-lens detector.

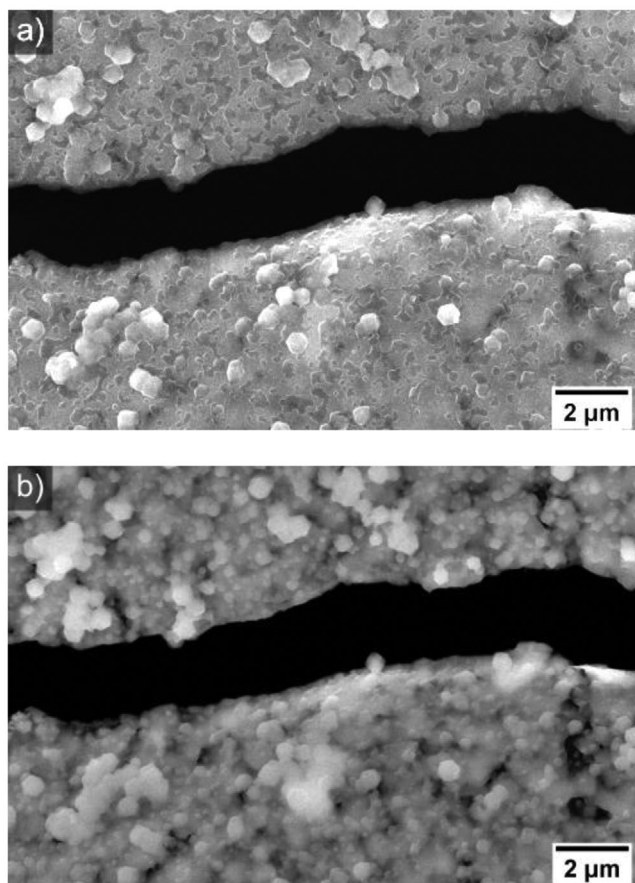


Figure 2. SEM micrographs of ZIF-8 obtained from layer-by-layer growth after 100 deposition cycles. Images were taken simultaneously at 10 keV primary electron energy with the a) through-lens detector and b) in-chamber Everhardt–Thornley detector. The film is ruptured in the center of the image (black region).

cycles, an almost closed ZIF-8 film has formed with some surface roughness and individual crystals protruding from the film. The film is ruptured in the center of the image (black region). The SEM image Figure 2b of the same region was taken with the in-chamber Everhardt–Thornley detector (ETD), which does not only reveal surface topography but also subsurface information. This image explains the origin of the film topography observed in Figure 2a. The film consists of ZIF-8 particles with a broad size distribution between some 10 nm

and around 500 nm that have coalesced and are additionally overgrown. Apart from the crack in the center of the image, there are some small dark regions left (mainly in a narrow stripe at the lower right side), where the carbon film remains visible. Interestingly, the comparison of Figures 1a and 2a shows that the deposited amount of ZIF-8 does not scale with the number of cycles during lbl growth but increases nonlinearly for the 100-cycle sample. However, Figures 1a and 2a demonstrate that ZIF-8 growth on aC film with UV/ozone treatment proceeds by nucleation and growth of crystals and formation of a closed film by crystal coalescence. It was earlier reported that during the formation of the crystalline ZIF-8 in form of powder in aqueous solutions, first the nucleation of the Zn and Hmim ions takes place to form the transient crystalline ZIF-8 state, followed by a rapid increase of the number of crystals, their further maturation, and intergrowth via the Ostwald ripening process.^[34] Based on our observations, it can be assumed that similar heterogeneous growth takes place also during lbl growth of ZIF-8 as SURMOF. Further investigations of this growth process, especially during the early stage, are ongoing.

2.3. Crystallinity

HRTEM was conducted to verify the crystalline structure of the ZIF-8 particles. For HRTEM, the preparation of ZIF-8 on a thin aC film is essential, because it only weakly affects the HRTEM contrast of ZIF-8. It also prevents damage that is caused if a ZIF-8, grown on a massive substrate, has to be transferred to an electron-transparent support for TEM studies. Hence, the synthesis procedure used here is advantageous. **Figure 3a** shows a HRTEM image of a ZIF-8 crystallite with a size of $240 \times 250 \text{ nm}^2$ after lbl growth for 50 deposition cycles. The nearly square shape of the particle is rounded at the corners. It is compatible with the RD particle shape in [010] projection. In fact, results obtained by electron tomography (cf. Figure 5) show that particles grow as half-particles with a flat interface on the aC film. We note that ZIF-8 is prone to electron-beam-induced radiation damage. In general, MOFs begin to lose their crystallinity if the cumulative dose reaches $10\text{--}20 \text{ electrons}/\text{Å}^2$,^[39] which limits the achievable specimen resolution and makes HRTEM imaging challenging.^[9,50] For this reason, the signal-to-noise ratio of the HRTEM image in Figure 3b was improved by average-background subtraction filtering.

A magnified region of the image reveals the crystallinity of the particle (Figure 3b). The periodicity in this image

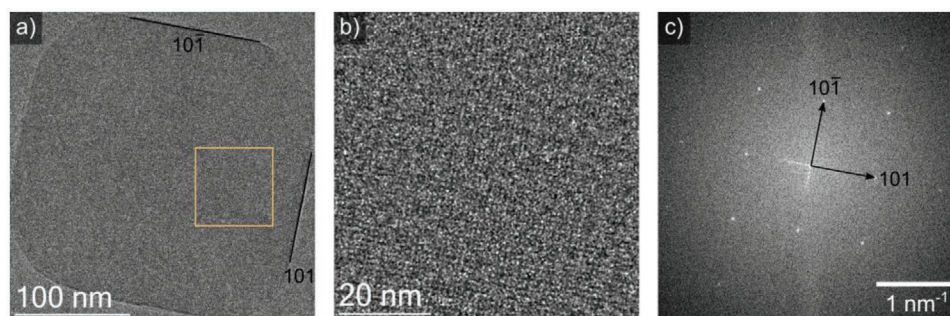


Figure 3. a) HRTEM image of a ZIF-8 crystallite on aC film after 50 deposition cycles, b) magnified image section of the marked area in (a) after average-background subtraction filtering. c) Fourier-transformed image (a) showing reflections that are compatible with the ZIF-8 [010] zone axis.

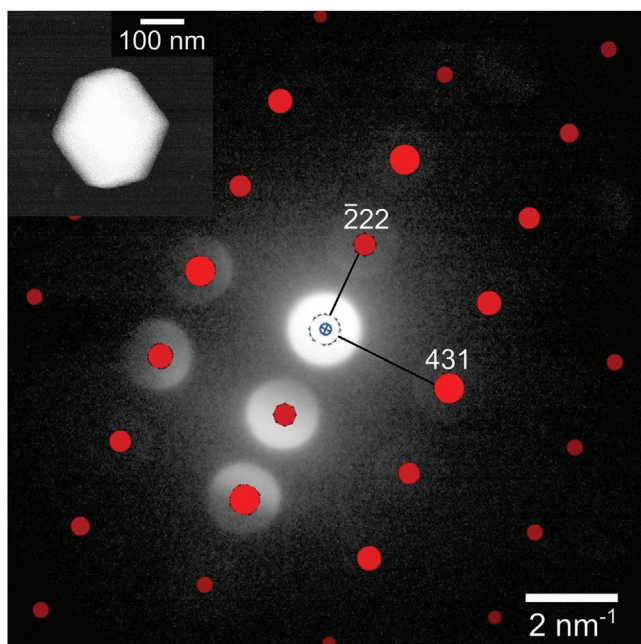


Figure 4. Nano-beam electron diffraction pattern of an Ag/ZIF-8 crystallite (50 deposition cycles). The diffraction pattern is overlaid by a simulated diffraction pattern of ZIF-8 in $[2\bar{5}7]$ zone axis. The inset HAADF-STEM image in the upper left corner shows the particle from which the diffraction pattern was taken.

corresponds to the expected cubic structure of ZIF-8 with space group $I\bar{4}3m$ (body-centered cubic), lattice parameter $a = 16.99 \text{ \AA}$, and composition $C_{24}H_{30}N_{12}O_{10}Zn_3$ ^[51] as revealed by the Fourier-transformed HRTEM image shown in Figure 3c. It shows $(10\bar{1})$ and (101) Bragg reflections up to the second order as expected for the $[010]$ zone axis of ZIF-8. The marked Bragg reflections of the $(10\bar{1})$ and (101) planes correspond to a lattice-plane distance of 1.19 nm, which is in good agreement with the theoretical pore size of ZIF-8. The HRTEM image of another particle is shown in Figure S6, Supporting Information.

Nano-beam electron diffraction (NBED) with a small beam convergence angle can also be used to study the crystalline structure of ZIF-8 nanocrystals without the necessity of a highly sensitive CMOS camera. NBED also facilitates the analysis of zone axes with lower symmetry. In this work, it was used to determine the structure of Ag/ZIF-8.

Figure 4 shows in the inset a HAADF-STEM image of a crystallite expected to be Ag/ZIF-8. The image was taken after the acquisition of the NBED pattern shown in Figure 4. The visible Bragg reflections are compatible with the simulated diffraction pattern of ZIF-8 in $[2\bar{5}7]$ zone axis overlaid on the experimental pattern. This demonstrates that the morphology and crystalline structure of ZIF-8 particles are not affected by the addition of Ag NPs formation cycles. We note that additional Bragg reflections expected from Ag NPs could not be observed.

2.4. 3D Reconstruction of Ag/ZIF-8 Particles

The lbl “ship-in-the-bottle” synthesis of Ag/ZIF-8 should ideally lead to a composite, which can be described as “one

nanoparticle @ one ZIF-8 pore.” Thus, very small ($<2 \text{ nm}$) nanoparticles are expected to form in the pores of ZIF-8, leading to a 3D arrangement of NPs in the ZIF-8 film. The visualization of the NP arrangement requires the use of electron tomography to reconstruct the 3D sample structure. Electron tomography allows in particular to distinguish whether NPs are embedded in ZIF-8 or whether they are located on the ZIF-8 surface.

The HAADF-STEM image in Figure 5a was taken from a tomographic tilt series of a ZIF-8 crystal. The projected shape is fully consistent with a RD particle viewed in $[111]$ direction (cf. Scheme 1b) although it looks like a cube in this projection. Some small bright dots are observed in the region of the ZIF-8 particle, which are tentatively assigned to Ag NPs. Many of them are also distributed around the ZIF-8 particle, apart from additional regions of contamination with a slightly enhanced intensity compared to the aC film. The NPs have a diameter between 2 and 4 nm.

After 3D reconstruction of the ZIF-8 particle from the tomographic tilt series, slices in all directions through the particle volume can be checked for the presence of Ag NPs (Figure 5b). Only few and not evenly distributed Ag NPs are found in the ZIF-8 crystal, marked by arrows in Figure 5b. The aC film covered with contamination and Ag NPs is seen in a side perspective and is marked by the red line. The tomogram in Figure 5c shows the surface of the 3D reconstructed volume. The 3D reconstruction of the particle (light blue) reveals that the crystal shape is not a complete rhombic dodecahedron, but only a half-particle. This indicates that the ZIF-8 crystals grow with a planar interface on the aC film and are firmly attached to it. The typical RD shape of the crystal further shows that ZIF-8 as SURMOF is not damaged by the contact with $AgNO_3$ and $NaBH_4$. The aC film is not visible in Figure 5c due to its weak scattering power, but a large amount of Ag NPs and contamination (red) deposited on the aC film can be observed. Figure 5d presents a top view on the particle which more clearly visualizes the RD particle shape. In Figure 5a, some NPs appear in the area of the ZIF-8 crystal, which can be interpreted as ZIF-8 with imbedded Ag NPs. The 3D reconstruction reveals though that most of the NPs are located underneath the ZIF-8 crystal—on the aC film—rather than inside the ZIF-8 particle. This exemplifies the vital importance of the tomography investigations to unambiguously determine the spatial distribution of the NPs within MOFs. A video of the 3D representation of the tomogram can be found in Supporting Information.

2.5. Composition (Elemental Analysis)

The elemental distribution of Ag/ZIF-8 was analyzed by EDXS with a special focus on the Ag distribution in/on the ZIF-8 particles and the surrounding region. In combination with HAADF-STEM tomography, EDXS can reveal whether Ag NPs are incorporated in the ZIF-8 particle or if they are located on the particle surface.

During EDXS mapping, where a large number of EDXS spectra is collected in a small area pixel-by-pixel, the sample is exposed to a high electron dose. ZIF-8 crystals tend to

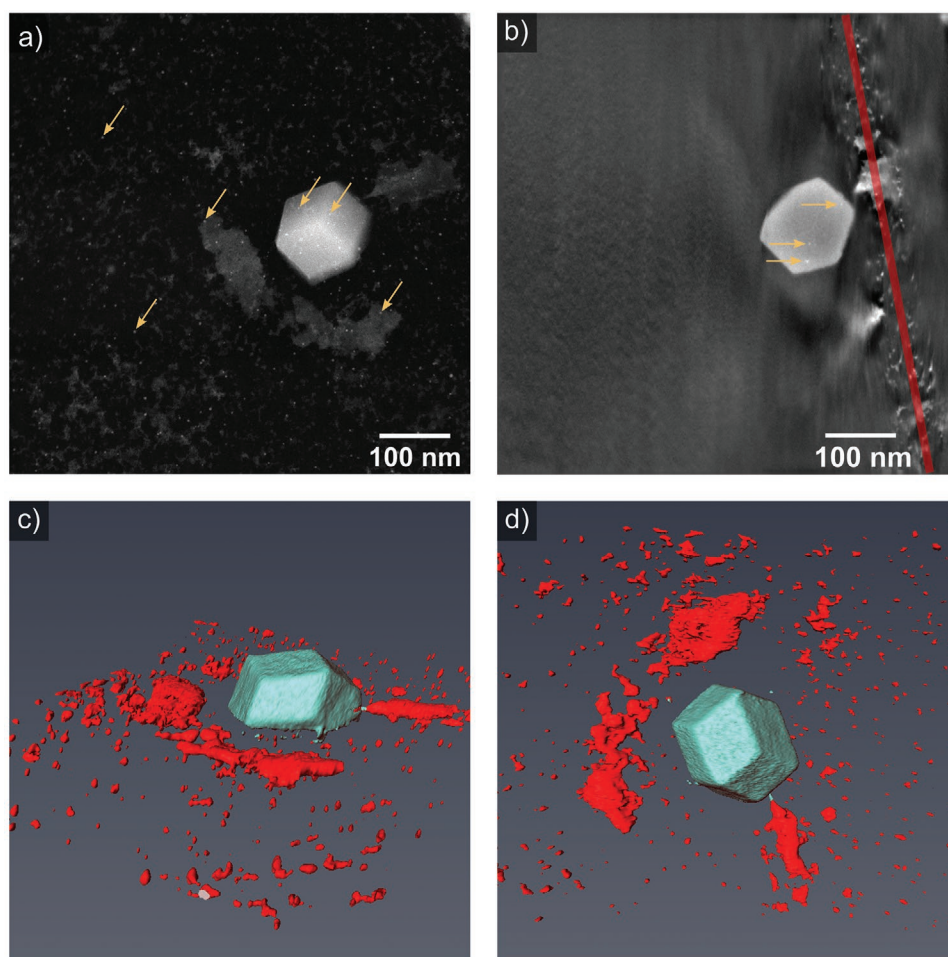


Figure 5. HAADF-STEM tomography of Ag/ZIF-8 (50 cycles ZIF-8, then 50 cycles Ag/ZIF-8). a) HAADF-STEM image from a tomographic tilt series at a small tilt angle. Bright spots (NPs, some marked by arrows) are visible in the area of the ZIF-8 particle, but also on the aC film. b) Slice through the reconstructed volume. A few NPs are incorporated in the crystal and are marked by arrows. The red line indicates the intersection between the plane of the aC film and the plane of the slice. c) 3D-surface representation of the tomogram with ZIF-8 indicated in light blue, NPs and contamination on the aC film in red. They mark the plane of the invisible aC film. d) Top view of the 3D-surface representation (video available in Supporting Information).

shrink even at a very low dose, which is a known problem for MOFs.^[52] However, they maintain the same distinctive shape, as indicated by comparison of images before and after a dose-intensive EDXS mapping (Figure S7, Supporting Information). Thus, EDXS mapping is possible under the chosen conditions.

Elemental distributions obtained by EDXS mapping of an Ag/ZIF-8 crystal are shown in Figure 6 for different elements. The octagonal contour is compatible with the truncated RD shape of ZIF-8, which is the shape-evolution step that precedes

the RD shape.^[35] Zn, N, and C are constituents of ZIF-8 and are found in the ZIF-8 particle. Moreover, some oxygen and sodium are also present in the material. They can both stem from the NaNO_3 , formed as the side product of the reduction of AgNO_3 with NaBH_4 , and stay tightly adsorbed in the ZIF-8 pores. Oxygen can also stem from the adsorbed water molecules, which is often the case for ZIF-8.^[4,53–55]

Particularly interesting with respect to the presence of Ag NPs is the Ag distribution, which does not show a higher

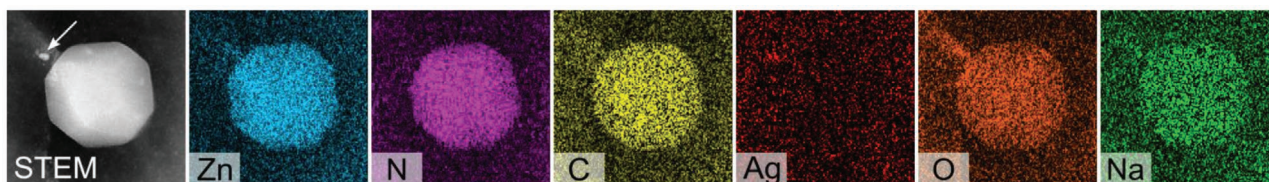


Figure 6. EDXS mapping of Ag/ZIF-8 (50 deposition cycles), showing a HAADF-STEM image of the ZIF-8 crystal and elemental maps for the particle. The width of each map is 238 nm. Zn, N, and C are regular constituents of ZIF-8 while O and Na are the remnants from the preparation process. The signal from Ag is low and only slightly enhanced for a small Ag particle (cf. arrow in the HAADF-STEM image).

Ag concentration in the region of the particle compared to the surrounding substrate. An enhancement of the Ag content would be expected if a significant amount of Ag would be present on the surface or within the particle. In combination with the HRTEM images and the NBED analysis it can be concluded that the intended preparation of Ag/ZIF-8 using lbl ship-in-the-bottle liquid impregnation allows to obtain highly crystalline ZIF-8 material. However, despite promising ToF-SIMS and XPS data (cf. Supporting Information), only negligible incorporation of Ag NPs within the ZIF-8 crystal could be achieved, as evidenced by STEM tomography (Figure 5) and EDXS (Figure 6). Instead, Ag-containing NPs cover the SURMOF support. This demonstrates again the importance of performing (S)TEM, tomography, and EDXS for the full analysis of guest/MOF composites.

3. Conclusions

Using a lbl preparation method, we were able to deposit ZIF-8 SURMOFs directly on commercial aC-covered grids for (S)TEM. This approach avoids the TEM sample preparation step, which is critical for MOF thin films and often leads to sample damage. The availability of such MOF thin films directly on TEM grids greatly facilitates the analysis of the as-synthesized MOFs and MOF crystallites by electron microscopy, since no further sample-preparation steps are required. Our method completely avoids damage and artifacts induced by sample preparation for (S)TEM, and is especially useful for surface-anchored MOFs. This preparation method permitted us to analyze for the first time an lbl-fabricated MOF, ZIF-8, without detachment of the material from a solid substrate. Reliable information about the material and its growth process could be obtained. A clear difference in the surface coverage of the ZIF-8 crystals on the aC film could be observed from the analysis of samples after 50 and 100 deposition cycles. This opens up the path to gain a deeper understanding of the lbl process of MOF formation, also during the early stages, where very little material is available and no XRD and CHNX analysis can be performed, and will be the subject of further investigations.

High-resolution (HR)TEM revealed the crystalline structure of ZIF-8. Still, the high sensitivity of ZIF-8 toward electron-beam damage impedes HRTEM imaging. On the other hand, nano-beam electron diffraction is a fast method to gain information on the crystalline structure and crystal orientation, which does not require a high-sensitivity electron camera. STEM tomography reveals the distinctive rhombic dodecahedral shape of layer-by-layer-grown ZIF-8 particles. The particles grow as half-particles with a planar interface on the carbon film.

Furthermore, we have tested a new lbl ship-in-the-bottle method to incorporate Ag nanoparticles (NPs) in ZIF-8. However, electron diffraction, tomography, and energy-dispersive X-ray spectroscopy mappings lead to the conclusion that few individual Ag NPs are incorporated in the ZIF-8. Homogenous incorporation of Ag NPs in ZIF-8 could not be achieved.

We expect this new and facile two-in-one synthesis and sample preparation method to stimulate more studies of MOFs, guest/MOF composites and mechanisms of their formation by electron microscopy.

4. Experimental Section

Materials: Methanol, anhydrous (max. 0.003% H₂O) for chromatography was purchased (Merck) and used without further purification. Zinc dinitrate hexahydrate 98%, 2-methyl-1H-imidazole 99%, 11-mercapto-1-undecanol (MUD) 99%, AgNO₃ ≥99% and NaBH₄ 99% were purchased (Alfa Aesar; Merck) and used without further purification.

Prefabricated TEM Cu grids covered by an aC film of 6–10 nm thickness were purchased from Plano GmbH (Wetzlar, product number S160A). The TEM grids were activated by UV irradiation with the UV/Ozone Procleaner from Bioforce Nanosciences, (IA-50010 USA) for 15 min resulting in a termination of the support surface by OH groups.

Synthesis: ZIF-8 fabrication: A dipping robot (MSM carousel stainer from SLEE Medical (Mainz)) was used to sequentially immerse the functionalized TEM grids in the methanolic solutions of the components and the rinsing liquids for defined times in the following order (Scheme 2a):

- 1) 10 mM zinc dinitrate hexahydrate solution (300 s),
- 2) pure methanol for rinsing (100 s),
- 3) 20 mM 2-methyl-1H-imidazole (300 s), and
- 4) pure methanol for rinsing (100 s).

This four-step procedure was then followed by the next deposition cycle starting with step (1). 50 and 100 cycles were applied to obtain ZIF-8 layers on TEM grids, suitable for analysis. After the deposition of ZIF-8 was finished, the sample was removed from the sample holder, rinsed with ethanol, dried at ambient conditions for 15 min and afterward stored in a vacuum desiccator.

The macro samples were prepared in the same way on Au-coated Si wafers, surface modified by immersion in a 1 mM ethanolic solution of MUD for 24 h at room temperature. Afterward, the wafers were rinsed with pure ethanol, dried under nitrogen flow, and used in the same reaction batch with TEM grids for ZIF-8 deposition.

Ag/ZIF-8 fabrication: the synthesis of these samples was performed using the same equipment. 50 cycles were deposited by immersing the TEM grid in the following methanolic solutions and the rinsing liquids for defined times in the following order (Scheme 2b):

- 1) 10 mM zinc dinitrate hexahydrate solution (300 s),
- 2) pure methanol for rinsing (100 s),
- 3) 20 mM 2-methyl-1H-imidazole (300 s),
- 4) pure methanol for rinsing (100 s),
- 5) 0.5 mM AgNO₃ solution (300 s),
- 6) pure methanol for rinsing (100 s),
- 7) 1 mM NaBH₄ solution (300 s), and
- 8) pure methanol for rinsing (100 s).

This eight-step procedure was then followed by the next deposition cycle starting with step (1). After the deposition of Ag/ZIF-8 was finished, the sample was removed from the sample holder, rinsed with ethanol, dried at ambient conditions for 15 min and afterward stored in a vacuum desiccator.

The macro samples for pXRD, IRRAS, ToF-SIMS, and XPS examination were prepared in the same way on Au-coated Si wafers, surface modified as described above. Functionalized macro samples were first sequentially immersed for 100 cycles of ZIF-8, following with 100 cycles of Ag/ZIF-8 fabrication. This way, 100 cycles ZIF-8 + 100 cycles Ag/ZIF-8 were applied to obtain a macro sample suitable for analysis with good signal-to-noise ratio.

Electron Microscopy: A Thermo Fisher Helios G4 FX NanoLab was used for SEM imaging. Surface topography information was obtained by using the TLD for secondary-electron detection. Collection of secondary-electrons with the in-chamber ETD yields not only surface topography but also subsurface information due to secondary-electron emission from the backside of the TEM sample. HRTEM and NBED were performed with a FEI Titan³ 80-300 (formerly FEI, now Thermo Fisher Scientific) operated at 300 kV, which is equipped with a field emission gun (FEG) and a spherical-aberration corrector in the imaging

lens system. HAADF-STEM tomography with the FEI Titan³ 80-300 was applied for 3D reconstruction of ZIF-8 crystals and their interior. A Tecnai Osiris (formerly FEI, now Thermo Fisher Scientific) operated at 200 kV was utilized for EDXS and elemental mapping. The instrument is equipped with a high-brightness FEG and a super-X EDXS detector system comprising four silicon drift detectors. More detailed information on the experimental conditions and computational procedures are given in Supporting Information.

Supporting Information

Supporting Information is available from the Wiley Online Library or from the author.

Acknowledgements

The authors acknowledge funding by the Deutsche Forschungsgemeinschaft (DFG, German Research Foundation) under Germany's Excellence Strategy–2082/1–390761711 and thank the Carl Zeiss Foundation for financial support. K.K. acknowledges the Ministry of Science, Research and Art Baden-Württemberg (Research Seed Capital (RISC) 2017). The authors thank Dr. Radian Popescu (Laboratory for Electron Microscopy (LEM), KIT, Karlsruhe) for help with the EDXS and HRTEM measurements and Johannes Schmiege (LEM, KIT, Karlsruhe) for assistance with HRTEM imaging. The ToF-SIMS analysis was performed by Alexander Welle at Laboratory for Microscopy and Spectroscopy of the Karlsruhe Nano Micro Facility (KNMF) at KIT, Karlsruhe. The XPS analysis was performed by Dr. Xiaojuan Yu and Dr. Yuemin Wang at Institute of Functional Interfaces at KIT, Karlsruhe. We acknowledge support by the KIT-Publication Fund of the Karlsruhe Institute of Technology.

Open access funding enabled and organized by Projekt DEAL.

Conflict of Interest

The authors declare no conflict of interest.

Author Contributions

M.H. and K.K. contributed equally to this work. D.G., C.W. and S.B. supervised the project. K.K. conceived the project and synthesized the samples. E.V.S. and S.M. synthesized the samples and conducted the XRD and IRRAS measurements of macro samples. M.H. performed the SEM and (S)TEM measurements and data analysis and wrote the main part of the manuscript with contributions from K.K. and all other authors. All authors read the manuscript and contributed to the discussions of the results.

Keywords

chemical composition analysis, electron microscopy, high spatial resolution, layer-by-layer growth, surface-anchored metal–organic frameworks, zeolitic imidazolate framework-8

Received: July 20, 2020

Revised: August 26, 2020

Published online:

[1] R. Banerjee, A. Phan, B. Wang, C. Knobler, H. Furukawa, M. O'Keeffe, O. M. Yaghi, *Science* **2008**, 319, 939.

- [2] D. Zou, D. Liu, J. Zhang, *Energy Environ. Mater.* **2018**, 1, 209.
- [3] B. Chen, Z. Yang, Y. Zhu, Y. Xia, *J. Mater. Chem.* **2014**, 2, 16811.
- [4] K. S. Park, Z. Ni, A. P. Côté, J. Y. Choi, R. Huang, F. J. Uribe-Romo, H. K. Chae, M. O'Keeffe, O. M. Yaghi, *Proc. Natl. Acad. Sci. USA* **2006**, 103, 10186.
- [5] J.-P. Zhang, A.-X. Zhu, R.-B. Lin, X.-L. Qi, X.-M. Chen, *Adv. Mater.* **2011**, 23, 1268.
- [6] A.-X. Zhu, R.-B. Lin, X.-L. Qi, Y. Liu, Y.-Y. Lin, J.-P. Zhang, X.-M. Chen, *Microporous Mesoporous Mater.* **2012**, 157, 42.
- [7] J. J. Beh, J. K. Lim, E. P. Ng, B. S. Ooi, *Mater. Chem. Phys.* **2018**, 216, 393.
- [8] R. F. Jofrishaal, R. Ediati, Y. Amri, *J. Phys.: Conf. Ser.* **2020**, 1460, 012086.
- [9] J. Cravillon, S. Münzer, S.-J. Lohmeier, A. Feldhoff, K. Huber, M. Wiebcke, *Chem. Mater.* **2009**, 21, 1410.
- [10] H. Zhang, Q. Shi, X. Kang, J. Dong, *J. Coord. Chem.* **2013**, 66, 2079.
- [11] H. Bux, F. Liang, Y. Li, J. Cravillon, M. Wiebcke, J. Caro, *J. Am. Chem. Soc.* **2009**, 131, 16000.
- [12] Q. Bao, Y. Lou, T. Xing, J. Chen, *Inorg. Chem. Commun.* **2013**, 37, 170.
- [13] V. V. Butova, A. P. Budnik, E. A. Bulanova, A. V. Soldatov, *Mendeleev Commun.* **2016**, 26, 43.
- [14] L. S. Lai, Y. F. Yeong, K. K. Lau, A. M. Shariff, *Procedia Eng.* **2016**, 148, 35.
- [15] P. J. Beldon, L. Fábíán, R. S. Stein, A. Thirumurugan, A. K. Cheetham, T. Frišćić, *Angew. Chem., Int. Ed.* **2010**, 49, 9640.
- [16] A. Martínez Joaristi, J. Juan-Alcañiz, P. Serra-Crespo, F. Kapteijn, J. Gascon, *Cryst. Growth Des.* **2012**, 12, 3489.
- [17] H.-Y. Cho, J. Kim, S.-N. Kim, W.-S. Ahn, *Microporous Mesoporous Mater.* **2013**, 169, 180.
- [18] B. Seoane, J. M. Zamaro, C. Tellez, J. Coronas, *CrystEngComm* **2012**, 14, 3103.
- [19] O. Shekhah, R. Swaidan, Y. Belmabkhout, M. Du Plessis, T. Jacobs, L. J. Barbour, I. Pinnau, M. Eddaoudi, *Chem. Commun.* **2014**, 50, 2089.
- [20] O. Shekhah, M. Eddaoudi, *Chem. Commun.* **2013**, 49, 10079.
- [21] V. Chernikova, O. Shekhah, M. Eddaoudi, *ACS Appl. Mater. Interfaces* **2016**, 8, 20459.
- [22] E. P. Valadez Sánchez, H. Gliemann, K. Haas-Santo, C. Wöll, R. Dittmeyer, *Chem. Ing. Tech.* **2016**, 88, 1798.
- [23] E. P. Valadez Sánchez, H. Gliemann, K. Haas-Santo, W. Ding, E. Hansjosten, J. Wohlgemuth, C. Wöll, R. Dittmeyer, *J. Membr. Sci.* **2020**, 594, 117421.
- [24] H. Cai, Y.-L. Huang, D. Li, *Coord. Chem. Rev.* **2019**, 378, 207.
- [25] Z.-P. Ni, J.-L. Liu, M. N. Hoque, W. Liu, J.-Y. Li, Y.-C. Chen, M.-L. Tong, *Coord. Chem. Rev.* **2017**, 335, 28.
- [26] J. Cui, S. Ren, B. Sun, S. Jia, *Coord. Chem. Rev.* **2018**, 370, 22.
- [27] Q. Yang, Q. Xu, H.-L. Jiang, *Chem. Soc. Rev.* **2017**, 46, 4774.
- [28] W. Xiang, Y. Zhang, H. Lin, C.-J. Liu, *Molecules* **2017**, 22, 2103.
- [29] F. Schröder, R. A. Fischer, *Top. Curr. Chem.* **2010**, 293, 77.
- [30] M. Meilikhov, K. Yusenko, D. Esken, S. Turner, G. van Tendeloo, R. A. Fischer, *Eur. J. Inorg. Chem.* **2010**, 2010, 3701.
- [31] H. R. Moon, D.-W. Lim, M. P. Suh, *Chem. Soc. Rev.* **2013**, 42, 1807.
- [32] D. Esken, S. Turner, O. I. Lebedev, G. van Tendeloo, R. A. Fischer, *Chem. Mater.* **2010**, 22, 6393.
- [33] Y. Jing, Q. Lei, C. Xia, Y. Guan, Y. Yang, J. He, Y. Yang, Y. Zhang, M. Yan, *RSC Adv.* **2020**, 10, 698.
- [34] M. Jian, B. Liu, R. Liu, J. Qu, H. Wang, X. Zhang, *RSC Adv.* **2015**, 5, 48433.
- [35] J. Cravillon, C. A. Schröder, H. Bux, A. Rothkirch, J. Caro, M. Wiebcke, *CrystEngComm* **2012**, 14, 492.
- [36] J. Troyano, A. Carné-Sánchez, C. Avci, I. Imaz, D. MasPOCH, *Chem. Soc. Rev.* **2019**, 48, 5534.
- [37] J. Cravillon, R. Nayuk, S. Springer, A. Feldhoff, K. Huber, M. Wiebcke, *Chem. Mater.* **2011**, 23, 2130.

- [38] G. Zhan, H. C. Zeng, *Nat. Commun.* **2018**, *9*, 3778.
- [39] D. Zhang, Y. Zhu, L. Liu, X. Ying, C.-E. Hsiung, R. Sougrat, K. Li, Y. Han, *Science* **2018**, *359*, 675.
- [40] Y. Zhu, J. Ciston, B. Zheng, X. Miao, C. Czarnik, Y. Pan, R. Sougrat, Z. Lai, C.-E. Hsiung, K. Yao, I. Pinnau, M. Pan, Y. Han, *Nat. Mater.* **2017**, *16*, 532.
- [41] C. Rösler, D. Esken, C. Wiktor, H. Kobayashi, T. Yamamoto, S. Matsumura, H. Kitagawa, R. A. Fischer, *Eur. J. Inorg. Chem.* **2014**, *2014*, 5514.
- [42] Z.-G. Gu, H. Fu, T. Neumann, Z.-X. Xu, W.-Q. Fu, W. Wenzel, L. Zhang, J. Zhang, C. Wöll, *ACS Nano* **2016**, *10*, 977.
- [43] M. Darbandi, H. K. Arslan, O. Shekhah, A. Bashir, A. Birkner, C. Wöll, *Phys. Status Solidi RRL* **2010**, *4*, 197.
- [44] J. Zhao, B. Gong, W. T. Nunn, P. C. Lemaire, E. C. Stevens, F. I. Sidi, P. S. Williams, C. J. Oldham, H. J. Walls, S. D. Shepherd, M. A. Browe, G. W. Peterson, M. D. Losego, G. N. Parsons, *J. Mater. Chem.* **2015**, *3*, 1458.
- [45] W. Guo, Z. Chen, C. Yang, T. Neumann, C. Kübel, W. Wenzel, A. Welle, W. Pfleging, O. Shekhah, C. Wöll, E. Redel, *Nanoscale* **2016**, *8*, 6468.
- [46] L. Heinke, M. Tu, S. Wannapaiboon, R. A. Fischer, C. Wöll, *Microporous Mesoporous Mater.* **2015**, *216*, 200.
- [47] H. Gliemann, C. Wöll, *Mater. Today* **2012**, *15*, 110.
- [48] H.-L. Jiang, T. Akita, T. Ishida, M. Haruta, Q. Xu, *J. Am. Chem. Soc.* **2011**, *133*, 1304.
- [49] X.-H. Liu, J.-G. Ma, Z. Niu, G.-M. Yang, P. Cheng, *Angew. Chem., Int. Ed.* **2015**, *54*, 988.
- [50] K. Murata, M. Wolf, *Biochim. Biophys. Acta* **2018**, *1862*, 324.
- [51] K. S. Park, Z. Ni, A. P. Cote, J. Y. Choi, R. Huang, F. J. Uribe-Romo, H. K. Chae, M. O'Keeffe, O. M. Yaghi, *CCDC 602542: Experimental Crystal Structure Determination*, Cambridge Crystallographic Data Centre, Cambridge **2006**.
- [52] C. Wiktor, M. Meledina, S. Turner, O. I. Lebedev, R. A. Fischer, *J. Mater. Chem. A* **2017**, *5*, 14969.
- [53] X.-C. Huang, Y.-Y. Lin, J.-P. Zhang, X.-M. Chen, *Angew. Chem., Int. Ed.* **2006**, *45*, 1557.
- [54] H.-P. Jing, C.-C. Wang, Y.-W. Zhang, P. Wang, R. Li, *RSC Adv.* **2014**, *4*, 54454.
- [55] W. Morris, C. J. Stevens, R. E. Taylor, C. Dybowski, O. M. Yaghi, M. A. Garcia-Garibay, *J. Phys. Chem. C* **2012**, *116*, 13307.